

# Overlapping morphological and functional properties between M4 and M5 intrinsically photosensitive retinal ganglion cells

Takuma Sonoda<sup>1,2</sup> | Yudai Okabe<sup>1</sup> | Tiffany M. Schmidt<sup>1</sup> 

<sup>1</sup>Department of Neurobiology, Northwestern University, Evanston, Illinois

<sup>2</sup>Northwestern University Interdepartmental Neuroscience Program, Northwestern University, Chicago, Illinois

## Correspondence

Tiffany M. Schmidt, Department of Neurobiology, Northwestern University, Evanston, IL.  
 Email: tiffany.schmidt@northwestern.edu

## Funding information

Alfred P. Sloan Foundation; Esther A. and Joseph Klingenstein Fund; National Institutes of Health, Grant/Award Number:  
 1DP2EY022584; National Institutes of Health, Grant/Award Numbers: EY030360-01, F31, EY025202, T32

## Abstract

Multiple retinal ganglion cell (RGC) types in the mouse retina mediate pattern vision by responding to specific features of the visual scene. The M4 and M5 melanopsin-expressing, intrinsically photosensitive retinal ganglion cell (ipRGC) subtypes are two RGC types that are thought to play major roles in pattern vision. The M4 ipRGCs overlap in population with ON-alpha RGCs, while M5 ipRGCs were recently reported to exhibit opponent responses to different wavelengths of light (color opponency). Despite their seemingly distinct roles in visual processing, previous reports have suggested that these two populations may exhibit overlap in their morphological and functional properties, which calls into question whether these are in fact distinct RGC types. Here, we show that M4 and M5 ipRGCs are distinct morphological classes of ipRGCs, but they cannot be exclusively differentiated based on color opponency and dendritic morphology as previously reported. Instead, we find that M4 and M5 ipRGCs can only be distinguished based on soma size and the number of dendritic branch points in combination with SMI-32 immunoreactivity. These results have important implications for clearly defining RGC types and their roles in visual behavior.

## KEY WORDS

alpha, color opponent, ipRGC, melanopsin, retina, retinal ganglion cell, RRID: AB\_143165, RRID: AB\_221569, RRID: AB\_2532130, RRID: AB\_2532130, RRID: AB\_2534072, RRID: AB\_2534096, RRID: AB\_2534098, RRID: AB\_2535804, RRID: AB\_2535812, RRID: AB\_2721225, RRID: AB\_2722769, RRID: AB\_300798, RRID: AB\_509997, RRID: SCR\_001622, RRID: SCR\_002798, RRID: SCR\_011323, subtype

## 1 | INTRODUCTION

Intrinsically photosensitive retinal ganglion cells (ipRGCs) express the photopigment melanopsin and consist of six subtypes (termed M1–M6) (Berson, Dunn, & Takao, 2002; Hattar, Liao, Takao, Berson, & Yau, 2002; Quattrochi et al., 2019; Schmidt, Chen, & Hattar, 2011). Though they make up <10% of total RGCs, ipRGCs mediate and regulate a wide range of visual behaviors and physiological processes including: circadian photoentrainment, the pupillary light reflex, hormonal regulation, mood regulation, and image-formation (Brown, 2016; Lazzerini Ospri, Prusky, & Hattar, 2017; LeGates, Fernandez, & Hattar, 2014; Sonoda & Schmidt, 2016). Each ipRGC subtype has a

defining complement of intrinsic physiological properties, morphological characteristics, central projections, and, likely, behavioral roles. Thus, establishing reliable and reproducible criteria for classifying ipRGC subtypes is a crucial step for understanding how light information is ultimately processed to inform behavior.

Currently, most ipRGCs (M1, M2, M3, and M6) can be classified solely based on morphological properties (Lee & Schmidt, 2018; Quattrochi et al., 2019; Schmidt et al., 2011). However, the morphological and functional properties that define M4 and M5 ipRGCs remain less clear. M4 ipRGCs have recently been shown to overlap in population with ON-alpha RGCs (Schmidt et al., 2014), a conventional RGC type that has been widely studied across multiple species

(Manookin, Beaudoin, Ernst, Flagel, & Demb, 2008; Leo Peichl, 1991; Peichl, Ott, & Boycott Brian, 1987). ON-alpha RGCs in mice are commonly identified based on sustained increases in firing in response to light, SMI-32 immunoreactivity, large soma size, and large dendritic arbors (Baden et al., 2016; Bleckert, Schwartz, Turner, Rieke, & Wong, 2014; Coombs, van der List, Wang, & Chalupa, 2006; Duan et al., 2015; Krieger, Qiao, Rousso, Sanes, & Meister, 2017; Pang, Gao, & Wu, 2003; van Wyk, Wassle, & Taylor, 2009). On the other hand, M5 ipRGCs have classically been described as having “bushy” dendritic arbors and have recently been shown to have a unique functional feature: color opponency (Ecker et al., 2010; Stabio et al., 2018). Therefore, in principle, it is possible to differentiate the two based on dendritic arbor size and opponent responses to different wavelengths of light.

However, a recent report has shown that ON-alpha RGCs in the temporal retina exhibit bushy dendritic arbors and were proposed to correspond to M5 ipRGCs (Bleckert et al., 2014). Moreover, M5 ipRGCs identified in previous studies bear a strong resemblance to temporal ON-alpha RGCs and have even been reported to be SMI-32 immunoreactive (Ecker et al., 2010; Hu, Hill, & Wong, 2013; Lee & Schmidt, 2018). Other reports have also shown that ON-alpha RGCs located along the opsin-transition zone exhibit color opponent responses (Chang, Breuninger, & Euler, 2013) and that color opponency in M5 ipRGCs may depend on their location in the retina (Quattrochi et al., 2019). Therefore, these two criteria are potentially insufficient for providing reliable identification of M4 and M5 ipRGCs, which raises the question of whether these two populations are in fact anatomically and functionally distinct. Given the breadth and depth of study of alpha RGC function in visual neuroscience and the emerging understanding of ipRGC function in vision, it is critical to establish concrete criteria to distinguish these RGC types.

In this study, we examined the extent to which M4 and M5 ipRGCs can be differentiated based on morphological and functional properties. We find that M4 ipRGCs comprise a single RGC population and can be distinguished from M5 ipRGCs based on SMI-32 immunoreactivity. We further report that the dendritic morphology of bushy M4 ipRGCs in the temporal retina overlaps considerably with that previously reported for M5 ipRGCs. We also show that color opponency is not a defining feature of M5 ipRGCs as previously reported (Stabio et al., 2018) because both large and small M4 ipRGCs uniformly exhibit color opponent responses when recorded under light-adapted conditions. Moreover, the opponent responses of M4 ipRGCs match pharmacological features of those previously reported for M5 ipRGCs, suggesting that this is a state-dependent, rather than subtype-dependent feature of ipRGC signaling. These results demonstrate substantial overlap in the structural and functional properties of M4 and M5 ipRGCs while also identifying important defining features that can be used going forward to distinguish between these two populations.

## 2 | RESULTS

### 2.1 | The nasal-temporal scaling of SMI32+ ipRGC morphology matches that of ON-alpha RGCs

The dendritic field size of ON-alpha RGCs, which are SMI-32 immunoreactive (SMI-32+), have been shown to scale in size across the nasal-temporal axis of the retina with cells in the nasal retina having large dendritic arbors and cells in the temporal retina having smaller, bushy dendritic arbors (Bleckert et al., 2014). This led authors from this study to suggest that M4 ipRGCs could correspond to ON-alphas located in the nasal retina and M5 ipRGCs could correspond to bushier ON-alphas located in the temporal retina. This suggestion was supported by earlier reports showing M5 ipRGC examples consistent with temporal ON-alpha RGC morphology (Ecker et al., 2010; Hu et al., 2013; Lee & Schmidt, 2018) and reports of M5 ipRGCs being a “rare” population of cell when researchers randomly targeted ipRGCs for patch clamp recording in *Opn4<sup>Cre</sup>*; Z/EG animals (Ecker et al., 2010; Hu et al., 2013; Zhao, Stafford, Godin, King, & Wong, 2014). However, more recent reports have suggested that M4 ipRGCs overlap in population with all ON-alpha RGCs (Estevez et al., 2012; Rheaume et al., 2018; Schmidt et al., 2014; Sonoda, Lee, Birnbaumer, & Schmidt, 2018) and that the M5 ipRGC population is distinct from ON-alpha RGCs based on their smaller soma size and distribution throughout the entire retina (Reifler et al., 2015; Stabio et al., 2018). To distinguish between these two possibilities, we wanted to determine whether the properties of SMI-32+ ipRGCs match those previously reported for ON-alpha RGCs (i.e., all ON-stratifying, SMI-32+ cells; Bleckert et al., 2014) as a whole.

We first assessed whether the morphological properties of SMI-32+ ipRGCs exhibit the same nasal-temporal scaling reported for ON-alpha RGCs. To do this, we used two approaches to visualize the dendritic arbors and cell bodies of these cells. We first used an unbiased approach to sparsely label ipRGCs by making intravitreal injections of adeno-associated virus (AAVs) at a low titer in order to visualize individual dendritic arbors of ipRGCs (Supporting Information Figure S1). Specifically, we intravitreally injected AAV2/hSyn-DIO-hM3D-mCherry virus into the eyes of *Opn4<sup>Cre</sup>* mice. This AAV drives Cre-dependent expression of Gq-DREADDs tagged with mCherry, which allows for clear visualization of dendrites because Gq-DREADDs are membrane bound. We then immunolabeled for SMI-32 and reconstructed the arbors of all mCherry/SMI-32 double positive ipRGCs. We next took a targeted approach to reconstruct the arbors of SMI32+ ipRGCs by making intracellular recordings from ipRGCs with large somata in the *Opn4<sup>Cre/+</sup>*; Z/EG mouse line (in which all ipRGC subtypes express green fluorescent protein [GFP]) (Ecker et al., 2010; Novak, Guo, Yang, Nagy, & Lobe, 2000) while including Neurobiotin tracer in the pipette to allow for reconstruction of the dendritic arbors following recording (Figure 1a,b). We then immunolabeled these retinas for SMI-32 and reconstructed the arbors of filled, SMI-32+ ipRGCs. In both approaches, we recorded the location of each cell in the retina.

We then quantified the dendritic field diameter of SMI-32+ ipRGCs labeled with these two methods as a function of their position along the nasal-temporal axis of the retina and found that, like ON-alpha RGCs,

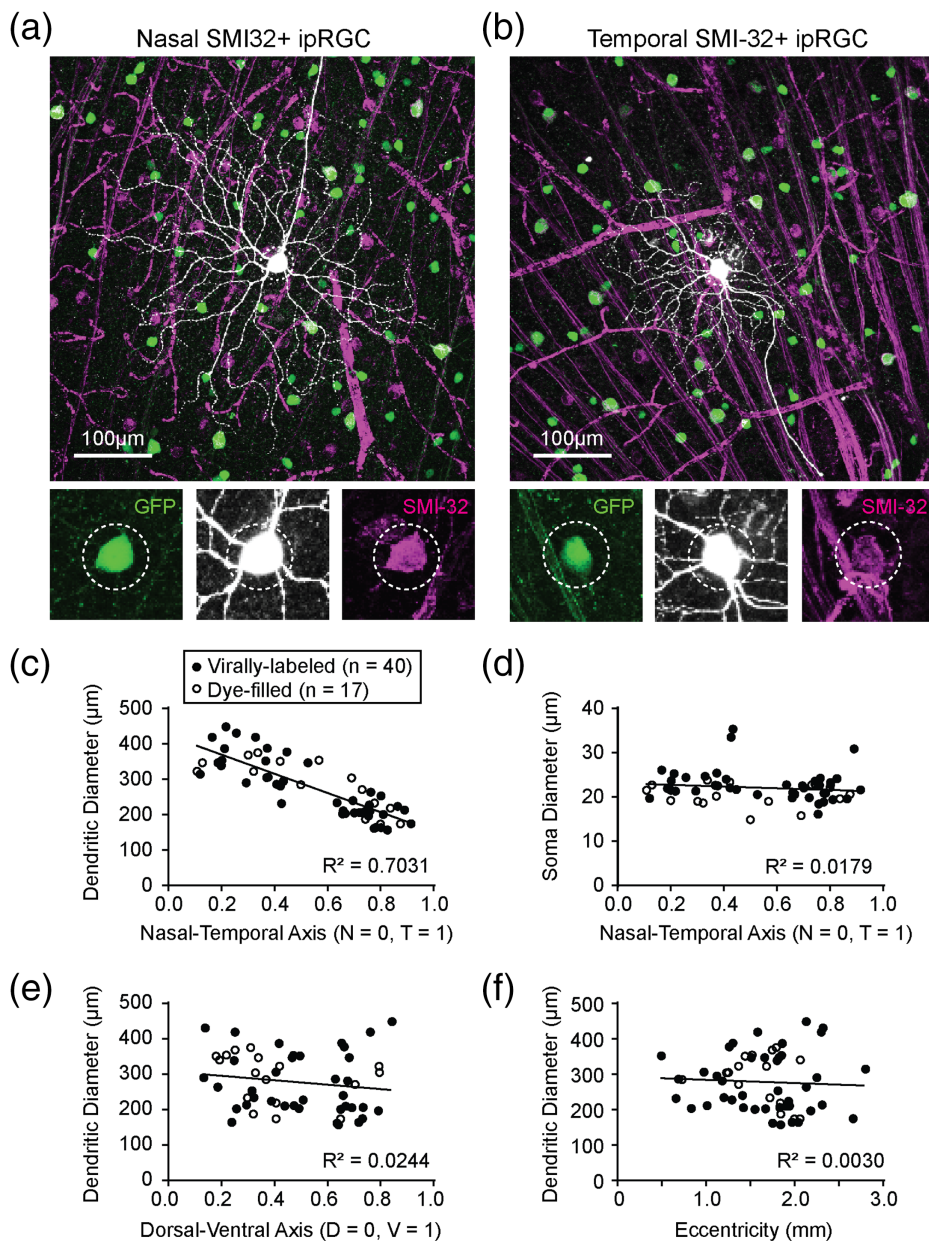


**FIGURE 1** The dendritic field size of SMI32+ ipRGCs decreases along the nasal-temporal axis of the retina. (a, b) Example images of two dye-filled SMI-32+ ipRGCs located in the nasal (a) and temporal (b) retina. Cells were targeted for patch clamp recording in *Oprn4<sup>Cre/+</sup>; Z/EG* retinas (in which all ipRGC subtypes express GFP). The area around the soma is enlarged in the bottom panels to show that the cells are both GFP+ and SMI-32+. Note that SMI-32+ ipRGCs in the nasal retina have large dendritic arbors and SMI-32+ ipRGCs in the temporal retina have more compact, bushy dendritic arbors. Scale bar represents 100 μm. (c) The dendritic diameter of SMI-32+ ipRGCs as a function of position along the nasal-temporal axis of the retina. Black circles indicate cells that were labeled by sparsely labeling ipRGCs using AAVs and open circles indicate cells that were filled with Neurobiotin tracer during patch clamp recording (see methods). The dendritic diameter of SMI-32+ ipRGCs scales linearly along the nasal-temporal axis as described previously for ON-alpha RGCs (Bleckert et al., 2014). (d) The soma diameter of SMI-32+ ipRGCs as a function of position along the nasal-temporal axis. Soma size did not correlate with position along the nasal-temporal axis indicating that no ipRGCs with small somata were SMI-32+. (e) The dendritic diameter of SMI-32+ ipRGCs as a function of position along the dorsal-ventral axis of the retina. Dendritic diameter did not correlate with position along the nasal-temporal axis. (f) The dendritic diameter of SMI-32+ ipRGCs as a function of eccentricity (distance from optic nerve head). The dendritic field diameter of SMI-32+ ipRGCs did not correlate with eccentricity. ipRGC, intrinsically photosensitive retinal ganglion cell; RGC, retinal ganglion cell [Color figure can be viewed at [wileyonlinelibrary.com](http://wileyonlinelibrary.com)]

their dendritic field diameter decreased linearly along the nasal-temporal axis (Figure 1a–c). Importantly, the soma size of SMI-32+ ipRGCs did not correlate with position along the nasal-temporal axis even when randomly labeled with AAV (Figure 1d), indicating that SMI-32+ ipRGCs

across the entire retina have large somata. Additionally, the dendritic field diameter of SMI-32+ ipRGCs did not correlate with overall eccentricity or position along the dorsal-ventral axis, which is consistent with ON-alpha RGCs (Figure 1e,f, Bleckert et al., 2014).

We next wanted to determine whether the retinal distribution of SMI-32+ ipRGCs matches that previously reported for the ON-alpha RGC population, which exhibits higher densities in the temporal retina (Bleckert et al., 2014). To do this, we immunolabeled the retinas of *Opn4<sup>Cre/+</sup>; Z/EG* mice for SMI-32. We then counted and marked the location of cells that were both GFP+ and SMI-32+ across the entire retina (Figure 2a). Like ON-alpha RGCs (Bleckert et al., 2014), SMI-32+ ipRGCs exhibit a density gradient across the nasal-temporal axis of the retina and are more densely distributed in the temporal retina (Figure 2a-d).

## 2.2 | SMI-32 positive ipRGCs are a single RGC type that correspond to the M4 ipRGC subtype

If all ON-alpha RGCs represent a single subtype (M4 ipRGCs), then they should exhibit a mosaic distribution in both the nasal and temporal

quadrants of the retina. To test this directly, we measured the coordinates of SMI-32+ ipRGCs in 1 mm<sup>2</sup> regions of the nasal and temporal retina as previously described (Bleckert et al., 2014; Rodieck, 1991). We then calculated a density recovery profile (DRP) which plots the density of cells around each reference cell in a 1 mm<sup>2</sup> region. If SMI-32+ ipRGCs are distributed in a mosaic manner, we would expect a zone of exclusion around each reference cell, indicated by a low cell density around each cell. Indeed, we found that SMI-32+ ipRGCs display a zone of exclusion in both the nasal and temporal quadrants of the retina (Figure 2c,d), though the size of this zone is reduced in temporal retina, in agreement with previous reports (Bleckert et al., 2014). These data indicate SMI-32+ ipRGCs represent a single RGC subtype, and argue against M4 ipRGCs representing the nasal ON-alpha RGCs and M5 ipRGCs representing the temporal ON-alpha RGCs.

We next tested whether temporal and nasal ON-alpha RGCs express similar molecular markers, as would be expected if they

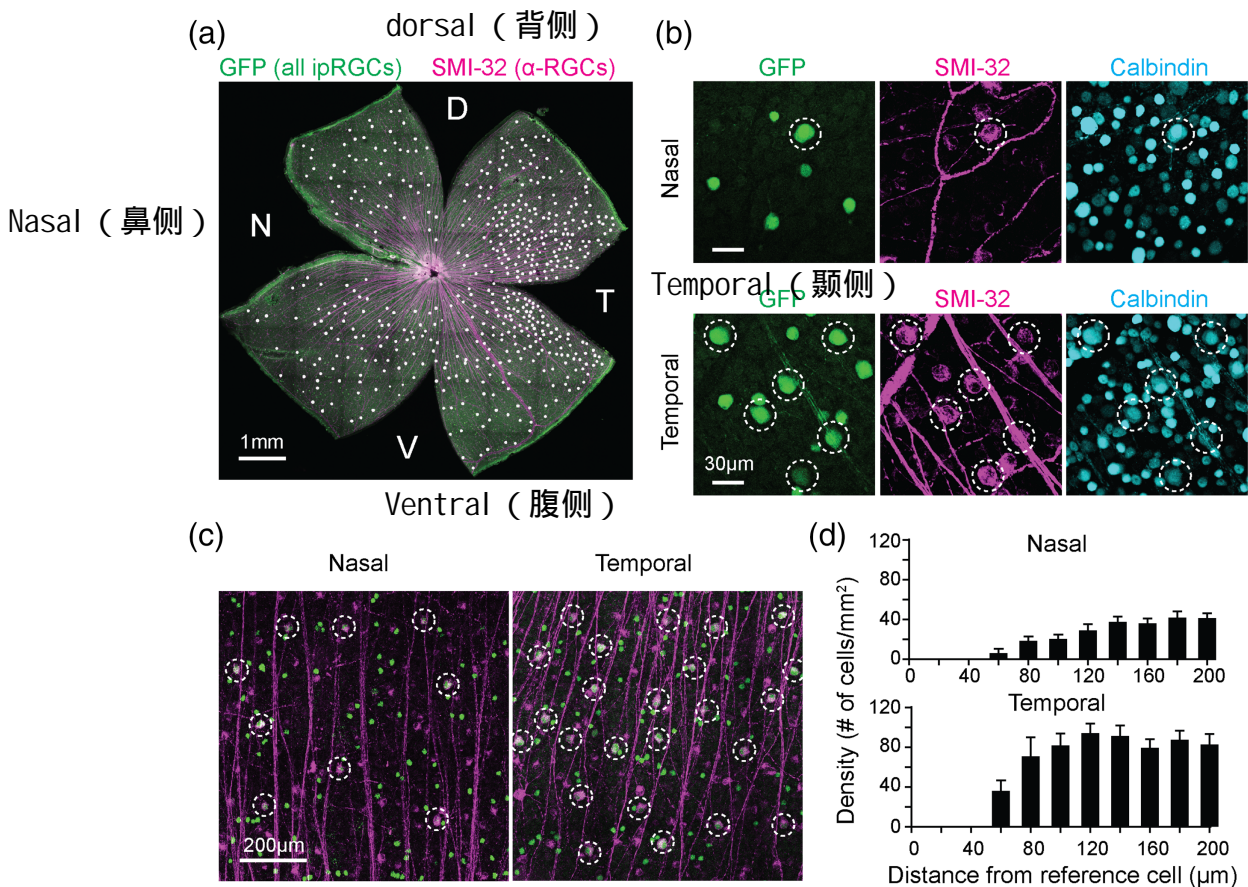


**FIGURE 2** SMI-32+ ipRGCs represent a single RGC type that corresponds to ON-alpha RGCs. (a) The distribution of SMI-32+ ipRGCs across the retina. White dots represent SMI-32+ cells labeled in *Opn4<sup>Cre/+</sup>; Z/EG* retinas (in which all ipRGC subtypes express GFP). Note that like ON-alpha RGCs, SMI-32+ ipRGCs are more densely distributed in the temporal retina. D (dorsal), N (nasal), V (ventral), and T (temporal). Scale bar represents 1 mm. (b) SMI-32+ ipRGCs in the nasal (top) and temporal (bottom) retina were immunostained for calbindin (cyan), which selectively labels ON-sustained alpha RGCs among the alpha RGCs. A total of 96% of SMI-32+ ipRGCs across the retina were calbindin immunoreactive (509/529 cells from five retinas), indicating that they share the same molecular identity as ON-sustained alpha RGCs described previously. Scale bar represents 30 μm. (c) Example: 1 mm<sup>2</sup> fields of view of the nasal (left) and temporal (right) retina in *Opn4<sup>Cre/+</sup>; Z/EG* mice. Dotted circles represent locations of SMI-32+ ipRGCs. Scale bar represents 200 μm. (d) Density recovery profiles of SMI-32+ ipRGCs in 1 mm<sup>2</sup> fields of view of the nasal (top) and temporal (bottom) retina. Data are mean ± SEM. Notice that there is a zone of exclusion around cells in both the nasal and temporal retina, indicating that SMI-32+ ipRGCs exhibit a mosaic distribution and represent a single RGC type. ipRGC, intrinsically photosensitive retinal ganglion cell; RGC, retinal ganglion cell [Color figure can be viewed at [wileyonlinelibrary.com](http://wileyonlinelibrary.com)]

represent a single population. Specifically, we assessed whether SMI-32+ ipRGCs are all immunoreactive for calbindin, which has been previously shown to selectively label ON-sustained alpha RGCs among the alpha RGCs (Krieger et al., 2017). To do this, we immunostained *Opn4<sup>Cre/+</sup>*; Z/EG retinas for SMI-32 and calbindin and measured the percentage of SMI-32 positive ipRGCs (GFP+ and SMI-32+) that were calbindin immunoreactive. We found that ~96% of SMI-32 positive ipRGCs (509/529 cells counted from five retinas) were calbindin immunoreactive (Figure 2b), providing further support for SMI-32+ ipRGCs representing regional variants of a single RGC type. Based on these findings, we propose that all SMI-32+ ipRGCs are in fact part of the M4 subtype, which corresponds to the ON-sustained alpha RGC, and that M5 ipRGCs are not represented within the SMI-32+ ipRGC population. Therefore, these findings suggest that M4 and M5

ipRGCs are distinct ipRGC subtypes and identify a marker that can be used to concretely distinguish between M4 (SMI-32+) and M5 (SMI-32-) ipRGCs.

**TABLE 1** Morphological properties of M4 and M5 intrinsically photosensitive retinal ganglion cell (ipRGCs)

	Nasal M4	Temporal M4	M5 <sup>a</sup>
Soma diameter ( $\mu\text{m}$ )	$23.1 \pm 2.4$	$21.3 \pm 3.1$	$14.2 \pm 2.4$
Dendritic diameter ( $\mu\text{m}$ )	$370.8 \pm 54.1$	$207.6 \pm 29.5$	$223.7 \pm 43.9$
Total branch points	$27.4 \pm 4.7$	$30.4 \pm 6.2$	$52.1 \pm 12.5$
Number of primary dendrites	$5.9 \pm 0.7$	$5.0 \pm 1.2$	$4.1 \pm 1.3$

Note: Data represent mean  $\pm$  SD. M4 ipRGC data are from the same cells in Figure 3.

<sup>a</sup>M5 ipRGC data are from Stabio et al., 2018.

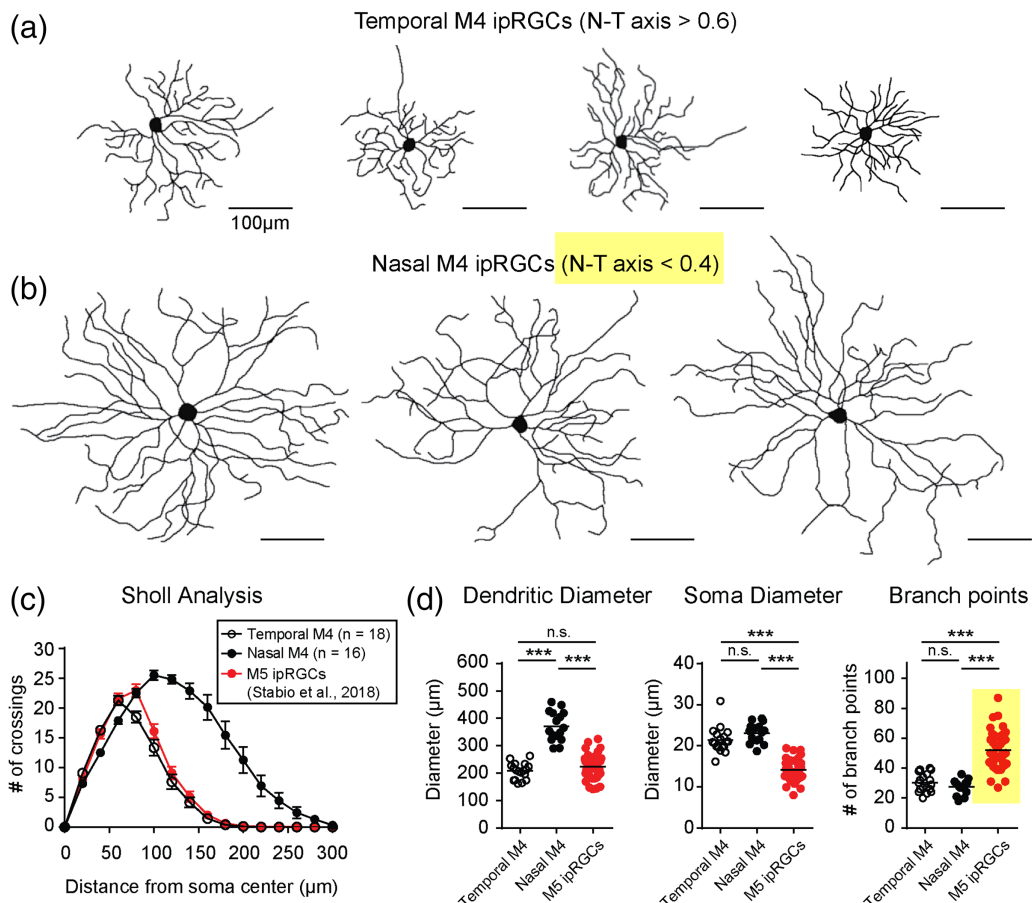


**FIGURE 3** The dendritic morphology of M4 ipRGCs in the temporal retina resembles that of M5 ipRGCs. (a, b) Example tracings of M4 ipRGCs (SMI-32+ ipRGCs) located in the temporal (a) and nasal (b) retina. Cells were grouped into temporal and nasal groups by selecting cells that were located along the normalized nasal-temporal axes between 0.6–1 and 0–0.4, respectively (see methods). (c) Sholl analyses of temporal M4 ipRGCs (open circles), nasal M4 ipRGCs (black circles), and M5 ipRGCs (red, replotted from Stabio et al., 2018). Note that Sholl profiles of temporal M4 ipRGCs and M5 ipRGCs exhibit considerable overlap. Data represent mean  $\pm$  SEM. (d) Grouped data showing the dendritic field diameter, soma diameter, and the number of branch points of temporal M4 ipRGCs (open circles), nasal M4 ipRGCs (black circles), and M5 ipRGCs (red circles, replotted from Stabio et al., 2018). The solid horizontal lines represent the mean. Cells are the same as those represented in the Sholl analysis in panel C. The dendritic field diameter of M5 ipRGCs significantly differed from nasal M4 ipRGCs ( $p < .001$ ), but not temporal M4 ipRGCs ( $p = .3900$ ). The soma diameter of M5 ipRGCs was significantly smaller than both temporal and nasal M4 ipRGCs ( $p < .001$ ). The number of branch points of M5 ipRGCs was significantly larger than both temporal and nasal M4 ipRGCs ( $p < .001$ ). ipRGC, intrinsically photosensitive retinal ganglion cell [Color figure can be viewed at [wileyonlinelibrary.com](http://wileyonlinelibrary.com)]

### 2.3 | The dendritic morphology of temporal M4 ipRGCs resembles that reported for M5 ipRGCs

The small, bushy dendritic arbors of temporal M4 ipRGCs resembles the dendritic arbor properties reported within the literature for M5 ipRGCs, and may lead to confusion when distinguishing between these two subtypes. We next sought to perform an in-depth morphological analysis to determine the extent of overlap between the properties of bushy, temporal M4 ipRGCs and the properties recently reported for M5 ipRGCs (Stabio et al., 2018).

We first divided M4 ipRGCs into nasal and temporal groups by selecting cells that were located 0.0–0.4 and 0.6–1.0 along the normalized nasal-temporal axis, respectively. We then performed a Sholl analysis to compare the branching patterns of nasal and temporal M4 ipRGCs with those previously reported for M5 ipRGCs (data replotted from Stabio et al., 2018) (Figure 3a–c). We found that the Sholl profiles and dendritic diameter of temporal M5 ipRGCs overlapped considerably with temporal M4 ipRGCs (Figure 3c,d, Table 1). However, the soma size of both nasal and temporal M4 ipRGCs was significantly

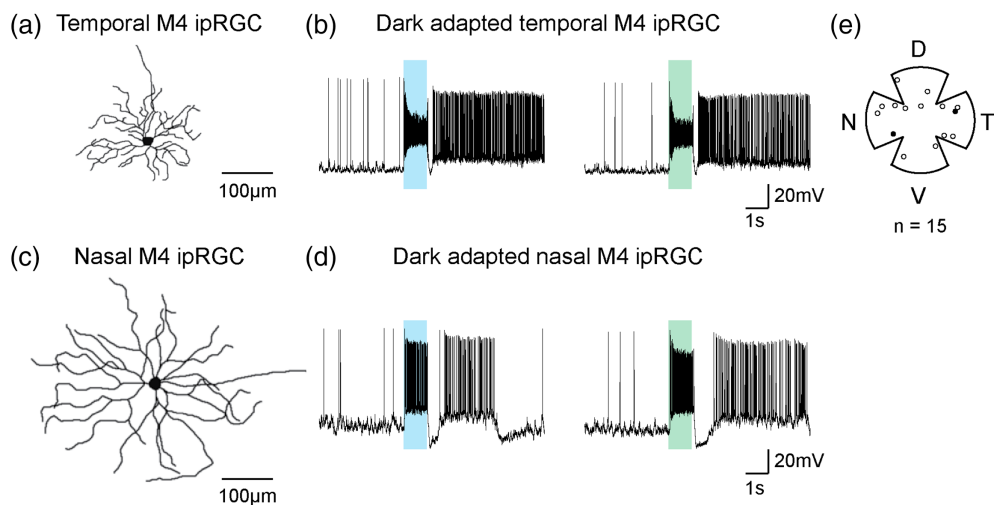
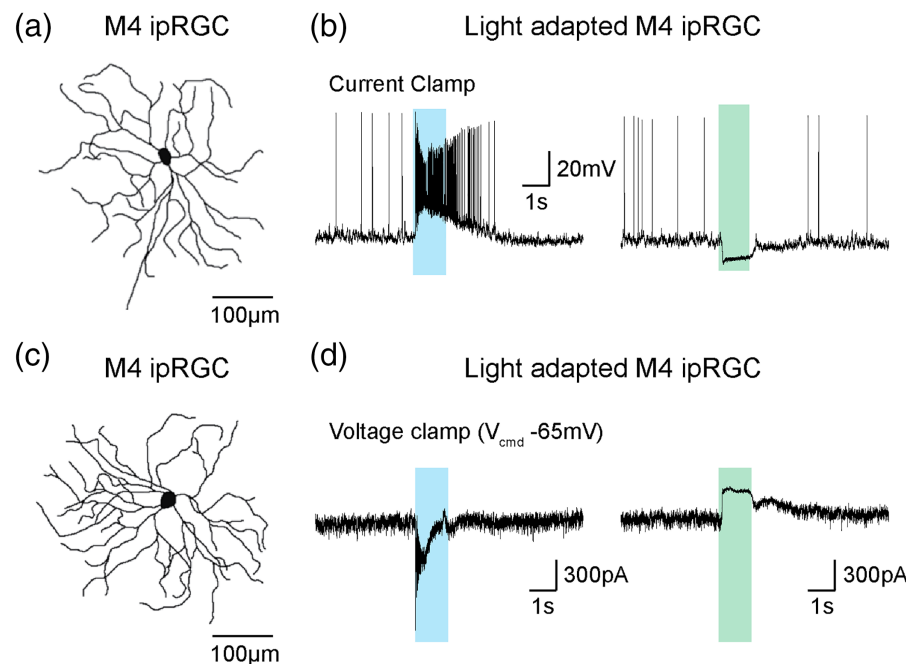


**FIGURE 4** M4 ipRGCs are not color opponent in dark-adapted conditions. (a, c) Tracings of M4 ipRGCs located in the temporal (a) and nasal (c) retina. These tracings correspond to cells used for example recordings in panels (b) and (d). (b, d) Example recordings from temporal (b) and nasal (d) M4 ipRGCs identified using 2-photon excitation in *Opn4<sup>Cre/+</sup>*; Z/EG retinas. Cells were exposed to full-field blue (470 nm, left) and green (540 nm, right) light stimuli (13.1 log quanta/cm<sup>2</sup>/s) from darkness. Dark-adapted M4 ipRGCs depolarized in response to both blue and green light indicating that they are not color opponent in these conditions. (e) A retina schematic with the locations of M4 ipRGCs recorded in dark-adapted conditions. The black dots represent locations of example cells in panels (a)–(d). ipRGC, intrinsically photosensitive retinal ganglion cell [Color figure can be viewed at wileyonlinelibrary.com]

**FIGURE 5** M4 ipRGCs exhibit color opponent responses in light-adapted conditions. (a, c) Tracings of M4 ipRGCs that correspond to cells used for example recordings in panels (b) and (d). (b, d) Example recordings from light-adapted M4 ipRGCs recorded in current clamp (b) and voltage clamp (d) modes. In this experiment, M4 ipRGCs were identified using LED epifluorescence in *Opn4<sup>Cre/+</sup>*; Z/EG retinas (see methods). Cells were exposed to full-field blue (470 nm, left) and green (540 nm, right) light stimuli (13.1 log quanta/cm<sup>2</sup>/s) from darkness. In light-adapted conditions, M4 ipRGCs are inhibited by green light as evidenced by hyperpolarizing responses measured in current clamp (b) and outward current measured in voltage clamp (d). ipRGC, intrinsically photosensitive retinal ganglion cell [Color figure can be viewed at wileyonlinelibrary.com]



larger than that reported for M5 ipRGCs (Figure 3d) and the number of dendritic branch points of nasal and temporal M4 ipRGCs was significantly lower than that reported for M5 ipRGCs (Figure 3d, Table 1). These findings identify two morphological properties, soma size and the number of branch points, that differentiate temporal M4 ipRGCs from M5 ipRGCs.

To ensure that morphological comparisons between studies were valid, we attempted to target M5 ipRGCs in *Opn4*<sup>Cre/+</sup>; Z/EG retinas. We specifically targeted ON-stratifying ipRGCs with small somata for patch clamp recording and subsequently confirmed that cells were SMI-32 negative using immunohistochemistry. Of the 27 cells we targeted, we found that 6 morphologically resembled M5 ipRGCs and were SMI-32 negative (Figure S2). These results further confirm that

M5 ipRGCs are a distinct ipRGC subtype that can be robustly identified based on soma size, the number of branch points, and lack of SMI-32 immunoreactivity.

## 2.4 | Color opponent responses of M4 ipRGCs depend on light adaptation state

Previous work has suggested that color opponency is a defining functional feature of M5 ipRGCs (Stabio et al., 2018). Therefore, as a further test of separation between temporal M4 ipRGCs and M5 ipRGCs, we next tested whether temporal or nasal M4 ipRGCs are color opponent. To do this, we targeted M4 ipRGCs for patch clamp recording in *Opn4*<sup>Cre/+</sup>; Z/EG retinas using 2-photon excitation to

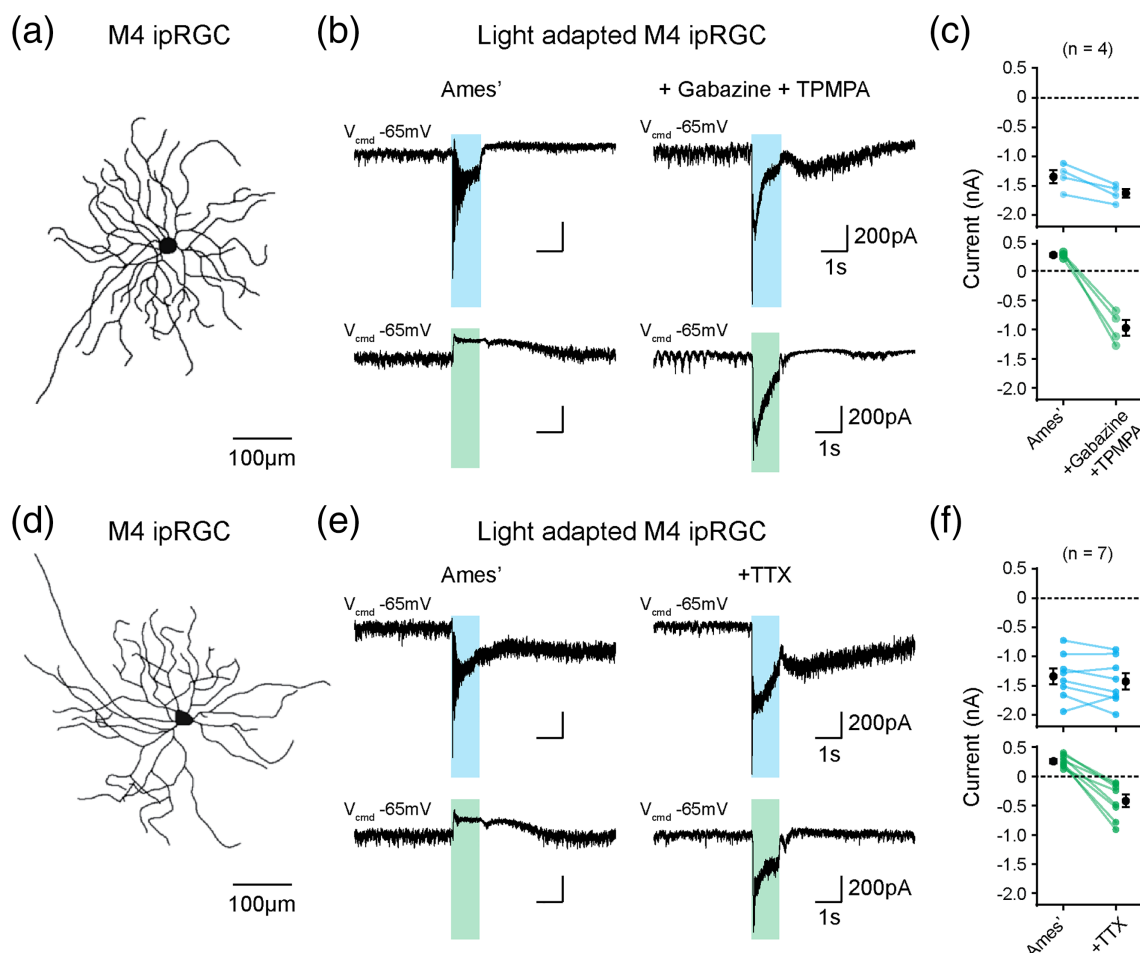


**FIGURE 6** Color opponent responses in light-adapted M4 ipRGCs are mediated by GABAergic spiking amacrine cells. (a,d) Tracings of M4 ipRGCs that correspond to cells used for example recordings in panels (b) and (e). (b) Example voltage clamp recordings from a light-adapted M4 ipRGC in response to full-field blue (470 nm, top) and green (540 nm, bottom) light stimuli (13.1 log quanta/cm<sup>2</sup>/s) from darkness. Responses were first recorded in Ames' medium (left), then subsequently in the presence of Gabazine (20 μM) and TPMPA (50 μM) (right). The outward current in response to green light reverses in polarity in the presence of Gabazine and TPMPA. (c) Grouped data showing maximum evoked current in response to blue (top) and green (bottom) light before (left) and after (right) application of Gabazine and TPMPA. The black dots and error bars represent mean ± SEM. (e) Example voltage clamp recordings from a light-adapted M4 ipRGC in response to full-field blue (470 nm, top) and green (540 nm, bottom) light stimuli (13.1 log quanta/cm<sup>2</sup>/s) from darkness. Responses were first recorded in Ames' medium (left), then subsequently in the presence of TTX (500 nM) (right). TTX also reverses the polarity of the outward current in response to green light. (f) Grouped data showing maximum evoked current in response to blue (top) and green (bottom) light before (left) and after (right) application of TTX. The black dots and error bars represent mean ± SEM. ipRGC, intrinsically photosensitive retinal ganglion cell [Color figure can be viewed at [wileyonlinelibrary.com](http://wileyonlinelibrary.com)]

maintain the cells in a dark-adapted state (see methods). We then exposed cells to blue (470 nm) and green (540 nm) light stimuli of equivalent light intensities (13.1 log quanta/cm<sup>2</sup>/s) from darkness. As expected, when we measured M4 ipRGC responses to these two different wavelengths of light in current clamp mode, we found that dark-adapted M4 ipRGCs across the entire retina showed no color opponency as evidenced by depolarizing responses to both stimuli (Figure 4). Thus, M4 ipRGCs are not color opponent in dark-adapted conditions.

We next performed experiments identical to those described earlier except that we identified GFP expressing M4 ipRGCs using bright, epifluorescent illumination to mimic prior recording conditions for M5 ipRGCs (Stabio et al., 2018). Though we expected to see a lack of color opponency in light-adapted M4 ipRGCs, we instead found that these cells were uniformly color opponent. Specifically, under light-adapted conditions, all M4 ipRGCs, regardless of their morphological characteristics (17/17 cells recorded), displayed opponent responses: depolarizing to blue light but hyperpolarizing to green light (Figure 5a,b). We then performed identical experiments, but in voltage clamp mode while holding cells at -65 mV. Consistent with our current clamp recordings, we observed an inward current in M4 ipRGCs in response to blue light, but an outward current in the same cell in response to green light (Figure 5c,d). These data indicate that in light-adapted conditions, color opponency is not a property exclusive to M5 ipRGCs.

We next wanted to determine whether color opponent responses of M4 ipRGCs in light-adapted conditions were driven by similar circuits as those described for M5 ipRGCs. In M5 ipRGCs, antagonistic responses to green light are driven by spiking GABAergic amacrine cells (Stabio et al., 2018). Therefore, in M5 ipRGCs, bath application of GABA receptor antagonists (Gabazine and TPMPA) and TTX reverses the polarity of responses to green light (Stabio et al., 2018). We tested whether these same pharmacological agents would similarly reverse the polarity of inhibitory responses for M4 ipRGCs in response to green light. To do this, we made voltage-clamp recordings from light-adapted M4 ipRGCs identified using epifluorescence in *Opn4*<sup>Cre/+</sup>; Z/EG retinas. We voltage clamped cells at -65 mV and recorded the response of each cell to blue and green lights first in control conditions and then in the presence of bath applied GABA receptor antagonists (Gabazine and TPMPA, Figure 6a-c) or TTX (Figure 6d-f) in the same cell. Consistent with the results reported for opponent responses of M5 ipRGCs, we found that GABA receptor antagonists and TTX each reversed the polarity of the outward current of M4 ipRGCs in response to green light (Figure 6). These data indicate that the antagonistic responses of M4 ipRGCs to green light are likely driven by spiking GABAergic amacrine cells, and that the light adaptation-dependent color opponency we observe in M4 ipRGCs arises from the same circuit level changes driving M5 ipRGC opponency.

### 3 | DISCUSSION

While ipRGCs were first appreciated for their roles in subconscious visual behaviors, a growing body of evidence has demonstrated that

ipRGCs also make an important contribution to image-forming vision (Allen et al., 2014; Allen, Storchi, Martial, Bedford, & Lucas, 2017; Barnard, Hattar, Hankins, & Lucas, 2006; Estevez et al., 2012; Milosavljevic et al., 2018; Schmidt et al., 2014; Storchi et al., 2015; Storchi et al., 2017; Zele, Adhikari, Cao, & Feigl, 2019). M4 and M5 ipRGCs have emerged as important ipRGC subtypes that participate in the image-forming pathway, but it is still unclear how to definitively distinguish between these subtypes. Given the high degree of overlap in the morphological properties of these subtypes, bushy, temporal M4 ipRGCs have quite possibly been included in previous analyses of M5 ipRGCs (Ecker et al., 2010; Hu et al., 2013; Lee & Schmidt, 2018; Quattrochi et al., 2019; Reifler et al., 2015; Stabio et al., 2018; Zhao et al., 2014), highlighting the need for concrete distinguishing features to define these subtypes, especially given that the alpha RGCs and ipRGCs are among the most widely studied RGC types. Moreover, the capability to reliably identify and differentiate RGC subtypes is critical for understanding how each RGC contributes to visual behavior and for consistency and reproducibility in future studies of ON-alpha RGCs (M4 ipRGCs) and M5 ipRGCs. Here, we clarify important features that distinguish between M4 and M5 ipRGCs as well as identify previously unrecognized points of structural and functional overlap (Figure 7).

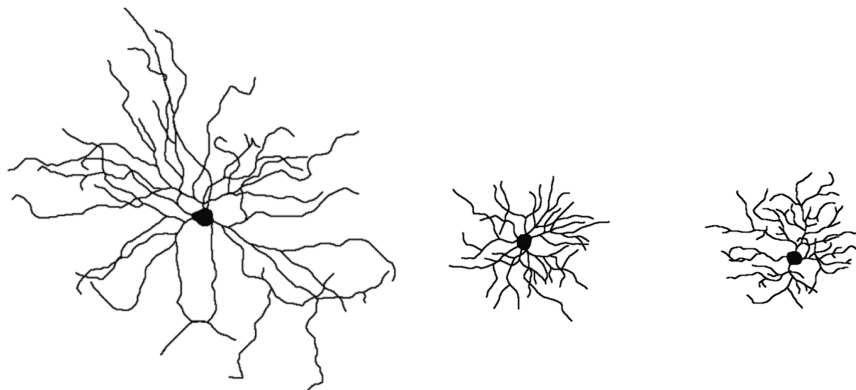
#### 3.1 | Identification of M4 versus M5 ipRGCs

Our results indicate that all SMI-32+ ipRGCs represent a single RGC population that corresponds to the ON-alpha RGCs described previously (Figures 1-3). Therefore, we propose that all SMI-32+ ipRGCs be included in the M4 ipRGC subtype. In addition, our data clearly show that dendritic morphology alone cannot be used to easily differentiate M4 and M5 ipRGCs as has been done in the past (Ecker et al., 2010; Hu et al., 2013; Zhao et al., 2014) because M4 ipRGCs (SMI-32+) located in the temporal 40% of the retina have dendritic morphologies that significantly overlap with M5 ipRGCs described previously (Figure 3). Our data suggest that soma size and the number of dendritic branch points may be used to differentiate M4 and M5 ipRGCs (Figure 3d). However, there is still overlap in soma sizes and the number of branch points between M4 and M5 ipRGCs (Figure 3d), which indicates that these parameters should not exclusively be used by researchers going forward, but instead be combined with SMI-32 immunoreactivity when differentiating between M4 (SMI-32+) and M5 (SMI-32-) ipRGCs (Figure 7).

#### 3.2 | Distribution of M4 and M5 ipRGCs

Previous reports have suggested that M4 and M5 ipRGCs are more densely distributed in the ventral retina (Hughes, Watson, Foster, Peirson, & Hankins, 2013), which is seemingly inconsistent with our results showing that M4 ipRGCs are more densely distributed in the temporal retina (Figures 1 and 2). This discrepancy is likely explained by the distribution patterns of recently discovered M6 ipRGCs that were unaccounted for in earlier studies. A recent study has shown that M6 ipRGCs are more densely distributed in the ventral retina





	Nasal M4 ipRGC	Temporal M4 ipRGCs	M5 ipRGCs
Dendritic arbor size	Large ( $370.8 \pm 54.1 \mu\text{m}$ )	Small, bushy ( $207.6 \pm 29.5 \mu\text{m}$ )	Small, bushy ( $223.7 \pm 43.9 \mu\text{m}$ )
Soma size	Large ( $23.1 \pm 2.4 \mu\text{m}$ )	Large ( $21.3 \pm 3.1 \mu\text{m}$ )	Small ( $14.2 \pm 2.4 \mu\text{m}$ )
Number of branch points	Small ( $27.4 \pm 4.7 \mu\text{m}$ )	Small ( $30.4 \pm 6.2 \mu\text{m}$ )	Large ( $52.1 \pm 12.5 \mu\text{m}$ )
SMI-32 immunoreactivity	Positive	Positive	Negative
Color opponency in light-adapted tissue	Color opponent	Color opponent	Color opponent
Color opponency in dark-adapted tissue	Not color opponent <sup>†</sup>	Not color opponent <sup>†</sup>	??

**FIGURE 7** Summary of findings. Example tracings of a nasal M4 ipRGC, temporal M4 ipRGC, and M5 ipRGC (taken from Figures 3 and S2) and a table with parameters that can be used to differentiate M4 and M5 ipRGCs for future studies. Values listed in gray are taken from Table 1 and represent mean  $\pm$  SD. Values for dendritic arbor size and soma size are dendritic field diameter and soma diameter. M5 ipRGC data are from Stabio et al., 2018. <sup>†</sup>Note that M4 ipRGCs (ON-alpha RGCs) located along the opsin-transition zone are color opponent as described in Chang et al., 2013. ipRGC, intrinsically photosensitive retinal ganglion cell

(Quattrochi et al., 2019). However, the distribution patterns of M6 ipRGCs could also be a product of the *Cdh3-GFP* mouse line that was used to label M6 ipRGCs (Quattrochi et al., 2019). Further characterization of the distribution patterns of M5 and M6 ipRGCs is necessary to make more definitive conclusions about the distribution of M5 and M6 ipRGCs.

### 3.3 | Mechanisms of color opponency in light-adapted ipRGCs

Though color opponency has been reported to be a defining feature of M5 ipRGCs, we found that all M4 ipRGCs consistently exhibit color opponency when recording in similar, light-adapted conditions. M4 ipRGCs (ON-alpha RGCs) receive strong rod input (Grimes, Schwartz, & Rieke, 2014; Schroeder et al., 2018; Wang, Weick, & Demb, 2011), which provides excitatory drive in response to a light stimulus delivered from darkness. This pathway is likely significantly bleached by the full-field light that we used to identify M4 ipRGCs in

our “light-adapted” experiments (Figures 5 and 6), which would allow for the inhibitory response described previously from wide-field amacrine cells to dominate (Farrow et al., 2013). Recent work has also shown that the inhibitory surround of ON-alpha RGCs is most sensitive to green light stimuli, which may explain why this inhibition is prominent in response to green light (Joesch & Meister, 2016).

It is important to note that the “color opponency” we observed here is not the same color opponency reported in ON-alpha RGCs near the opsin-transition zone, which was tested using S- and M-cone isolating stimuli on an isoluminant background (Chang et al., 2013). In order to replicate the conditions under which M5 ipRGCs were color opponent (Stabio et al., 2018), we presented blue (470 nm) and green (540 nm) light steps from darkness. Our results suggest that the circuit mechanisms underlying color opponency in light-adapted M4 ipRGCs resembles that observed in M5 ipRGCs (Figure 6). This could explain variability in the color opponency of M5 cells reported in a separate study (Quattrochi et al., 2019). Alternatively, it is possible that M5 cells, unlike M4 cells, continue to exhibit color opponency in dark-adapted tissue.

Color opponent responses have been reported in brain regions that receive direct input from ipRGCs (Denman, Siegle, Koch, Reid, & Blanche, 2017; Hayter & Brown, 2018; Walmsley et al., 2015). However, it is still unknown whether these responses are driven by direct input from color opponent RGCs. Going forward, one important question that needs to be addressed is whether the color opponency detected *in vivo* and color discrimination measured at the behavioral level (Jacobs, Williams, & Fenwick, 2004) result from the color opponent responses of single RGCs, or whether the color opponency reported here is an artifact of the light-adapted, *in vitro* recording conditions.

## 4 | MATERIALS AND METHODS

### 4.1 | Animals

All experimental procedures were approved by the Animal Care and Use Committee at Northwestern University. *Opn4*<sup>Cre/+</sup>; Z/EG mice (Ecker et al., 2010; Novak et al., 2000) were used for experiments determining the distribution of M4 ipRGCs and for making intracellular recordings from M4 and M5 ipRGCs. *Opn4*<sup>Cre/+</sup> mice were used for experiments in which AAVs were intravitreally injected to sparsely label ipRGCs. All animals were on a mixed B6/129 background and were between 1 and 2.5 months of age. Both female and male mice were used for all experiments.

### 4.2 | Solutions for electrophysiology

Recordings were made in Ames' medium (Sigma) supplemented with 23 mM sodium bicarbonate. Stock solutions of tetrodotoxin citrate (Tocris, 10 mM), SR 95531 (Gabazine, Tocris, 25 mM), and TPMPA (Tocris, 100 mM) were made in water and added directly to Ames' medium for final concentrations of 500 nM for TTX, 20 µM for Gabazine, and 50 µM for TPMPA. The internal solution contained (in mM): 125 K-gluconate, 2 CaCl<sub>2</sub>, 2 MgCl<sub>2</sub>, 10 EGTA, 10 HEPES, 2 Na<sub>2</sub>-ATP, 0.5 Na-GTP, and 0.3% Neurobiotin (Vector Laboratories). 2 mM QX-314 chloride (Tocris) was added for voltage clamp experiments.

### 4.3 | In vitro retina preparation

Mice were dark-adapted overnight and anesthetized by intraperitoneal injection of 2,2,2-Tribromoethanol. Then, under dim red light, a 30 gauge needle was used to mark the nasal corneal margin. Mice were killed by cervical dislocation and the eyes were enucleated and transferred a petri dish with carbogenated (95% O<sub>2</sub>/5% CO<sub>2</sub>) Ames' medium. A large relieving cut was made in the nasal margin of the eye cup prior to removing the retina from the eye cup to keep track of retinal orientation. Retinas were then mounted onto a 12-mm poly-D-lysine coverslip (Corning). The coverslip was then mounted directly onto a recording chamber, anchored using a platinum ring with nylon mesh and placed on an electrophysiology rig. The retina was superfused with carbogenated Ames' medium (30–32°C) at 5–7 ml/min for

at least 30 min prior to recording. For experiments in which retinal location was not documented, retinas were sliced in half and incubated in a beaker with carbogenated Ames' medium (26°C) prior to mounting them on the electrophysiology rig.

### 4.4 | Electrophysiology and light stimulation

Infrared differential interference optics were used to visualize the ganglion cell layer of the retina. We identified M4 ipRGCs by locating cells with large somata (~20 µm) in *Opn4*<sup>Cre/+</sup>; Z/EG retinas and subsequently confirming whether they were GFP+ using either 2-photon excitation (910 nm) or LED epifluorescence (~480 nm, 13.5 log quanta/cm<sup>2</sup>/s). Retinas were exposed to the 2-photon laser or LED epifluorescence for typically less than 10 s using this approach. Cells were then always dark-adapted for at least 15 min prior to delivering any light stimulation. We found that this exposure level to LED light led to consistent opponent responses to blue versus green light. Of note, we found that exposing retinas to excessive LED epifluorescence (> 20 s) and/or to brighter LED epifluorescence (>15 log quanta/cm<sup>2</sup>/s) resulted in reversed polarity of the responses to both blue and green lights (data not shown). Fire-polished borosilicate pipettes (Sutter Instruments, 3–5 MΩ) were then used to target ipRGCs for recording. Data were collected using a Multiclamp 700B amplifier (Molecular Devices) with pClamp 10 acquisition software (Molecular Devices, RRID: SCR\_011323). Voltages were corrected for a –14 mV liquid junction potential calculated in pClamp.

Light stimuli were delivered using a DLP Light Crafter 4500 (Texas Instruments) projector through the condenser of the microscope. A diaphragm shutter (Thor labs) was placed in the path so that light delivery could be controlled by pClamp. A filter wheel (Thor labs) loaded with band-pass filters (470 and 540 nm, Thor Labs) and neutral density filters were also placed in the path to switch between blue and green light stimuli. To keep light adaptation as consistent as possible for every cell, only one to two cells were recorded per dark-adapted whole mount preparation and only one cell was recorded per piece in "light-adapted" experiments.

### 4.5 | Sparse viral labeling of ipRGCs

*Opn4*<sup>Cre/+</sup> mice between P30 and P40 were anesthetized by intraperitoneal injection of 2,2,2-Tribromoethanol. A hole was then punctured through the ora serrata using a 30 gauge needle. Each eye was then injected with 1 µL of AAV2/hSyn-DIO-hM3D(Gq)-mCherry (Addgene, viral prep #44361-AAV2) using a custom Hamilton syringe with a 33 gauge needle (Borghuis Instruments). AAVs were diluted to a titer of ~4 × 10<sup>10</sup> viral particles/ml using filtered PBS to achieve sparse labeling. Retinas for these experiments were dissected 1–3 weeks postinfection.

### 4.6 | Immunohistochemistry

Recorded retinas were fixed in 4% paraformaldehyde (Electron Microscopy Sciences) in PBS overnight at 4°C. Retinas were then washed for

1 hr in PBS at room temperature (RT) and subsequently blocked in 6% goat serum and 0.3% Triton in PBS. The retinas were then incubated in primary antibody solution containing rabbit anti-GFP (1:1000, Thermo, RRID: AB\_221569), mouse anti-SMI-32 (1:500, BioLegend, RRID: AB\_509997), and Streptavidin conjugated with Alexa 546 (1:500, Thermo, RRID: AB\_2532130) in blocking solution for two nights at 4°C. Then, the retinas were washed in PBS for 3 × 30 min at RT and then transferred to secondary antibody solution which contained Alexa 488 goat anti-rabbit (1:500, Thermo, RRID: AB\_143165), Alexa 647 goat anti-mouse (1:500, Thermo, RRID: AB\_2535804), and Streptavidin 546 (1:1000, Thermo, RRID: AB\_2532130) in blocking solution. Retinas were incubated in secondary antibody solution for 2–3 hr at RT and then washed in PBS for 3 × 30 min. Retinas were mounted on glass slides using Fluoromount aqueous mounting medium (Sigma).

In experiments examining the distribution of SMI-32 immunoreactive ipRGCs, retinas were dissected and fixed in 4% paraformaldehyde in PBS for 30 min at RT. The retinas were then washed for 1 hr at RT and subsequently incubated in 6% goat serum and 0.3% Triton in PBS overnight at 4°C. Retinas were incubated in primary antibody solution containing rabbit anti-GFP (1:1000) and mouse anti-SMI-32 (1:500) in blocking solution for two nights at 4°C. They were then washed in PBS for 3 × 30 min at RT and then transferred to secondary antibody solution which contained Alexa 488 goat anti-rabbit (1:500) and Alexa 647 goat anti-mouse (1:500) in blocking solution. Retinas were finally washed in PBS and mounted on glass slides using Fluoromount aqueous mounting medium.

In experiments determining whether SMI-32 immunoreactive ipRGCs were calbindin immunoreactive, retinas were processed in the same way except chicken anti-GFP (1:500, Abcam, RRID: AB\_300798), mouse anti-SMI-32 (1:500), and rabbit anti-calbindin (1:500, Swant, RRID: AB\_2721225) were included in the primary antibody solution and Alexa 488 goat anti-chicken (1:500, Thermo, RRID: AB\_2534096), Alexa 568 goat anti-mouse (1:500, Thermo, RRID: AB\_2534072), and Alexa 647 goat anti-rabbit (1:500, Thermo, RRID: AB\_2535812) were included in the secondary antibody solution. Retinas infected with AAVs were also processed in the same way except antibodies that were used to detect mCherry were added (chicken anti-mCherry, 1:500, Abcam, RRID: AB\_2722769 and Alexa 568 goat anti-chicken, 1:500, Thermo, RRID: AB\_2534098).

#### 4.7 | Data analysis

To determine the position of each cell along the nasal-temporal axis of the retina, we first measured the coordinates of the nasal and temporal poles of the retina in ImageJ. We then identified the coordinates of each labeled cell. We then calculated the equation of the line connecting the nasal and temporal poles, and determined the point along that line that was closest to each individual cell. Finally, we divided the distance for each of those points from the nasal pole by the total distance between the nasal and temporal poles to obtain a normalized position along the nasal-temporal axis. Thus, cells closer to the nasal pole would have a value closer to 0 and cells closer to the temporal pole would have a value closer to 1. Eccentricity was measured by

calculating the distance between the optic nerve head and the soma of each cell.

DRPs were calculated as previously described (Rodieck, 1991; Bleckert et al., 2014). Briefly, we obtained the coordinates of SMI-32 + ipRGCs in 1 mm<sup>2</sup> regions of the nasal and temporal retina. Then, the density of cells surrounding each reference cell was calculated in 20 μm bins using a custom script written in MATLAB (MathWorks, RRID: SCR\_001622). To eliminate edge effects, we only calculated the DRP of cells that were within the inner 60% of each 1 mm<sup>2</sup> region.

To trace the dendrites of M4 ipRGCs, we took maximum intensity projections of z-stack images taken using a Leica SPE5500 scanning confocal microscope. Then, the dendrites of M4 ipRGCs were traced using the NeuronJ plugin in ImageJ. Binary images were then produced and a Sholl analysis was performed by measuring the number of Sholl crossings with concentric circles increasing in 20 μm increments from the soma. All graphs and statistical analyses were performed using Graph Pad Prism 6 (RRID: SCR\_002798). To make multiple statistical comparisons, we first performed a one-way ANOVA followed by Tukey's post hoc test. Significance was concluded when  $p < .05$ .

#### ACKNOWLEDGMENTS

We would like to thank Dr. Marco Gallio and Dr. Gregory Schwartz for helpful comments on the manuscript and Dr. Samer Hattar for the gift of *Opn4*<sup>Cre</sup> mice. We would also like to thank Dr. Maureen Stabio for sharing M5 ipRGC raw data. This work was funded by an NIH grant 1DP2EY022584, a Sloan Research Fellowship in Neuroscience, and a Klingenstein-Simons Fellowship in the Neurosciences to T. M. S., NIH T32 EY025202 and NIH F31 EY030360-01 to support T. S., and a Northwestern University Summer Undergraduate Research Grant to support Y. O.

#### CONFLICT OF INTEREST

The authors declare no potential conflict of interest.

#### DATA AVAILABILITY STATEMENT

Source data are available from tiffany.schmidt@northwestern.edu upon request.

#### ORCID

Tiffany M. Schmidt  <https://orcid.org/0000-0002-4791-6775>

#### REFERENCES

- Allen, A. E., Storchi, R., Martial, F. P., Bedford, R. A., & Lucas, R. J. (2017). Melanopsin contributions to the representation of images in the early visual system. *Current Biology*, 27(11), 1623–1632 e1624. <https://doi.org/10.1016/j.cub.2017.04.046>

- Allen, A. E., Storchi, R., Martial, F. P., Petersen, R. S., Montemurro, M. A., Brown, T. M., & Lucas, R. J. (2014). Melanopsin-driven light adaptation in mouse vision. *Current Biology*, 24(21), 2481–2490. <https://doi.org/10.1016/j.cub.2014.09.015>
- Baden, T., Berens, P., Franke, K., Roman Roson, M., Bethge, M., & Euler, T. (2016). The functional diversity of retinal ganglion cells in the mouse. *Nature*, 529(7586), 345–350. <https://doi.org/10.1038/nature16468>
- Barnard, A. R., Hattar, S., Hankins, M. W., & Lucas, R. J. (2006). Melanopsin regulates visual processing in the mouse retina. *Current Biology*, 16(4), 389–395. <https://doi.org/10.1016/j.cub.2005.12.045>
- Berson, D. M., Dunn, F. A., & Takao, M. (2002). Phototransduction by retinal ganglion cells that set the circadian clock. *Science*, 295(5557), 1070–1073. <https://doi.org/10.1126/science.1067262>
- Bleckert, A., Schwartz, G. W., Turner, M. H., Rieke, F., & Wong, R. O. (2014). Visual space is represented by nonmatching topographies of distinct mouse retinal ganglion cell types. *Current Biology*, 24(3), 310–315. <https://doi.org/10.1016/j.cub.2013.12.020>
- Brown, T. M. (2016). Using light to tell the time of day: Sensory coding in the mammalian circadian visual network. *The Journal of Experimental Biology*, 219(Pt 12), 1779–1792. <https://doi.org/10.1242/jeb.132167>
- Chang, L., Breuninger, T., & Euler, T. (2013). Chromatic coding from cone-type unselective circuits in the mouse retina. *Neuron*, 77(3), 559–571. <https://doi.org/10.1016/j.neuron.2012.12.012>
- Coombs, J., van der List, D., Wang, G. Y., & Chalupa, L. M. (2006). Morphological properties of mouse retinal ganglion cells. *Neuroscience*, 140(1), 123–136. <https://doi.org/10.1016/j.neuroscience.2006.02.079>
- Denman, D. J., Siegle, J. H., Koch, C., Reid, R. C., & Blanche, T. J. (2017). Spatial organization of chromatic pathways in the mouse dorsal lateral geniculate nucleus. *The Journal of Neuroscience*, 37(5), 1102–1116. <https://doi.org/10.1523/JNEUROSCI.1742-16.2016>
- Duan, X., Qiao, M., Bei, F., Kim, I. J., He, Z., & Sanes, J. R. (2015). Subtype-specific regeneration of retinal ganglion cells following axotomy: Effects of osteopontin and mTOR signaling. *Neuron*, 85(6), 1244–1256. <https://doi.org/10.1016/j.neuron.2015.02.017>
- Ecker, J. L., Dumitrescu, O. N., Wong, K. Y., Alam, N. M., Chen, S. K., LeGates, T., ... Hattar, S. (2010). Melanopsin-expressing retinal ganglion-cell photoreceptors: Cellular diversity and role in pattern vision. *Neuron*, 67(1), 49–60. <https://doi.org/10.1016/j.neuron.2010.05.023>
- Estevez, M. E., Fogerson, P. M., Ilardi, M. C., Borghuis, B. G., Chan, E., Weng, S., ... Berson, D. M. (2012). Form and function of the M4 cell, an intrinsically photosensitive retinal ganglion cell type contributing to geniculocortical vision. *The Journal of Neuroscience*, 32(39), 13608–13620. <https://doi.org/10.1523/JNEUROSCI.1422-12.2012>
- Farrow, K., Teixeira, M., Szikra, T., Viney, T. J., Balint, K., Yonehara, K., & Roska, B. (2013). Ambient illumination toggles a neuronal circuit switch in the retina and visual perception at cone threshold. *Neuron*, 78(2), 325–338. <https://doi.org/10.1016/j.neuron.2013.02.014>
- Grimes, W. N., Schwartz, G. W., & Rieke, F. (2014). The synaptic and circuit mechanisms underlying a change in spatial encoding in the retina. *Neuron*, 82(2), 460–473. <https://doi.org/10.1016/j.neuron.2014.02.037>
- Hattar, S., Liao, H.-W., Takao, M., Berson, D. M., & Yau, K.-W. (2002). Melanopsin-containing retinal ganglion cells: Architecture, projections, and intrinsic photosensitivity. *Science*, 295(5557), 1065–1070. <https://doi.org/10.1126/science.1069609>
- Hayter, E. A., & Brown, T. M. (2018). Additive contributions of melanopsin and both cone types provide broadband sensitivity to mouse pupil control. *BMC Biology*, 16(1), 83. <https://doi.org/10.1186/s12915-018-0552-1>
- Hu, C., Hill, D. D., & Wong, K. Y. (2013). Intrinsic physiological properties of the five types of mouse ganglion-cell photoreceptors. *Journal of Neurophysiology*, 109(7), 1876–1889. <https://doi.org/10.1152/jn.00579.2012>
- Hughes, S., Watson, T. S., Foster, R. G., Peirson, S. N., & Hankins, M. W. (2013). Nonuniform distribution and spectral tuning of photosensitive retinal ganglion cells of the mouse retina. *Current Biology*, 23(17), 1696–1701. <https://doi.org/10.1016/j.cub.2013.07.010>
- Jacobs, G. H., Williams, G. A., & Fenwick, J. A. (2004). Influence of cone pigment coexpression on spectral sensitivity and color vision in the mouse. *Vision Research*, 44(14), 1615–1622. <https://doi.org/10.1016/j.visres.2004.01.016>
- Joesch, M., & Meister, M. (2016). A neuronal circuit for colour vision based on rod-cone opponency. *Nature*, 532(7598), 236–239. <https://doi.org/10.1038/nature17158>
- Krieger, B., Qiao, M., Roussel, D. L., Sanes, J. R., & Meister, M. (2017). Four alpha ganglion cell types in mouse retina: Function, structure, and molecular signatures. *PLoS One*, 12(7), e0180091. <https://doi.org/10.1371/journal.pone.0180091>
- Lazzerini Osprí, L., Prusky, G., & Hattar, S. (2017). Mood, the circadian system, and Melanopsin retinal ganglion cells. *Annual Review of Neuroscience*, 40, 539–556. <https://doi.org/10.1146/annurev-neuro-072116-031324>
- Lee, S. K., & Schmidt, T. M. (2018). Morphological identification of melanopsin-expressing retinal ganglion cell subtypes in mice. In N. Tanimoto (Ed.), *Mouse retinal phenotyping: Methods and protocols* (pp. 275–287). New York, NY: Springer New York.
- LeGates, T. A., Fernandez, D. C., & Hattar, S. (2014). Light as a central modulator of circadian rhythms, sleep and affect. *Nature Reviews Neuroscience*, 15(7), 443–454. <https://doi.org/10.1038/nrn3743>
- Manookin, M. B., Beaudoin, D. L., Ernst, Z. R., Flagel, L. J., & Demb, J. B. (2008). Disinhibition combines with excitation to extend the operating range of the OFF visual pathway in daylight. *The Journal of Neuroscience*, 28(16), 4136–4150. <https://doi.org/10.1523/JNEUROSCI.4274-07.2008>
- Milosavljevic, N., Storchi, R., Eleftheriou, C. G., Colins, A., Petersen, R. S., & Lucas, R. J. (2018). Photoreceptive retinal ganglion cells control the information rate of the optic nerve. *Proceedings of the National Academy of Sciences of the United States of America*, 115(50), E11817–E11826. <https://doi.org/10.1073/pnas.1810701115>
- Novak, A., Guo, C., Yang, W., Nagy, A., & Lobe, C. G. (2000). Z/EG, a double reporter mouse line that expresses enhanced green fluorescent protein upon cre-mediated excision. *Genesis*, 28(3–4), 147–155. [https://doi.org/10.1002/1526-968X\(200011/12\)28:3/4<147::AID-GENE90>3.0.CO;2-G](https://doi.org/10.1002/1526-968X(200011/12)28:3/4<147::AID-GENE90>3.0.CO;2-G)
- Pang, J.-J., Gao, F., & Wu, S. M. (2003). Light-evoked excitatory and inhibitory synaptic inputs to ON and OFF  $\alpha$  ganglion cells in the mouse retina. *The Journal of Neuroscience*, 23(14), 6063–6073. <https://doi.org/10.1523/jneurosci.23-14-06063.2003>
- Peichl, L. (1991). Alpha ganglion cells in mammalian retinae: Common properties, species differences, and some comments on other ganglion cells. *Visual Neuroscience*, 7(1–2), 155–169. <https://doi.org/10.1017/S0952523800011020>
- Peichl, L., Ott, H., & Boycott Brian, B. (1987). Alpha ganglion cells in mammalian retinae. *Proceedings of the Royal Society of London. Series B. Biological Sciences*, 231(1263), 169–197. <https://doi.org/10.1098/rspb.1987.0040>
- Quattrochi, L. E., Stabio, M. E., Kim, I., Ilardi, M. C., Michelle Fogerson, P., Leyrer, M. L., & Berson, D. M. (2019). The M6 cell: A small-field bis-tristratified photosensitive retinal ganglion cell. *The Journal of Comparative Neurology*, 527(1), 297–311. <https://doi.org/10.1002/cne.24556>
- Reifler, A. N., Chervenak, A. P., Dolikian, M. E., Benenati, B. A., Meyers, B. S., Demertzis, Z. D., ... Wong, K. Y. (2015). The rat retina has five types of ganglion-cell photoreceptors. *Experimental Eye Research*, 130, 17–28. <https://doi.org/10.1016/j.exer.2014.11.010>
- Rheaume, B. A., Jereen, A., Bolisetty, M., Sajid, M. S., Yang, Y., Renna, K., ... Trakhtenberg, E. F. (2018). Single cell transcriptome profiling of retinal ganglion cells identifies cellular subtypes. *Nature Communications*, 9(1), 2759. <https://doi.org/10.1038/s41467-018-05134-3>

- Rodieck, R. W. (1991). The density recovery profile: A method for the analysis of points in the plane applicable to retinal studies. *Visual Neuroscience*, 6(02), 95–111. <https://doi.org/10.1017/s095252380001049x>
- Schmidt, T. M., Alam, N. M., Chen, S., Kofuji, P., Li, W., Prusky, G. T., & Hattar, S. (2014). A role for melanopsin in alpha retinal ganglion cells and contrast detection. *Neuron*, 82(4), 781–788. <https://doi.org/10.1016/j.neuron.2014.03.022>
- Schmidt, T. M., Chen, S. K., & Hattar, S. (2011). Intrinsically photosensitive retinal ganglion cells: Many subtypes, diverse functions. *Trends in Neurosciences*, 34(11), 572–580. <https://doi.org/10.1016/j.tins.2011.07.001>
- Schroeder, M. M., Harrison, K. R., Jaeckel, E. R., Berger, H. N., Zhao, X., Flannery, M. P., ... Wong, K. Y. (2018). The roles of rods, cones, and melanopsin in photoresponses of M4 intrinsically photosensitive retinal ganglion cells (ipRGCs) and optokinetic visual behavior. *Frontiers in Cellular Neuroscience*, 12, 203. <https://doi.org/10.3389/fncel.2018.00203>
- Sonoda, T., Lee, S. K., Birnbaumer, L., & Schmidt, T. M. (2018). Melanopsin phototransduction is repurposed by ipRGC subtypes to shape the function of distinct visual circuits. *Neuron*, 99(4), 754–767 e754. <https://doi.org/10.1016/j.neuron.2018.06.032>
- Sonoda, T., & Schmidt, T. M. (2016). Re-evaluating the role of intrinsically photosensitive retinal ganglion cells: New roles in image-forming functions. *Integrative and Comparative Biology*, 56(5), 834–841. <https://doi.org/10.1093/icb/icw066>
- Stabio, M. E., Sabbah, S., Quattrochi, L. E., Ilardi, M. C., Fogerson, P. M., Leyrer, M. L., ... Berson, D. M. (2018). The M5 cell: A color-opponent intrinsically photosensitive retinal ganglion cell. *Neuron*, 97(1), 150–163 e154. <https://doi.org/10.1016/j.neuron.2017.11.030>
- Storchi, R., Bedford, R. A., Martial, F. P., Allen, A. E., Wynne, J., Montemurro, M. A., ... Lucas, R. J. (2017). Modulation of fast narrow-band oscillations in the mouse retina and DLGN according to background light intensity. *Neuron*, 93(2), 299–307. <https://doi.org/10.1016/j.neuron.2016.12.027>
- Storchi, R., Milosavljevic, N., Eleftheriou, C. G., Martial, F. P., Orlowska-Feuer, P., Bedford, R. A., ... Lucas, R. J. (2015). Melanopsin-driven increases in maintained activity enhance thalamic visual response reliability across a simulated dawn. *Proceedings of the National Academy of Sciences of the United States of America*, 112(42), E5734–E5743. <https://doi.org/10.1073/pnas.1505274112>
- van Wyk, M., Wassle, H., & Taylor, W. R. (2009). Receptive field properties of ON- and OFF-ganglion cells in the mouse retina. *Visual Neuroscience*, 26(3), 297–308. <https://doi.org/10.1017/S0952523809990137>
- Walmsley, L., Hanna, L., Mouland, J., Martial, F., West, A., Smedley, A. R., ... Brown, T. M. (2015). Colour as a signal for entraining the mammalian circadian clock. *PLoS Biology*, 13(4), e1002127. <https://doi.org/10.1371/journal.pbio.1002127>
- Wang, Y. V., Weick, M., & Demb, J. B. (2011). Spectral and temporal sensitivity of cone-mediated responses in mouse retinal ganglion cells. *The Journal of Neuroscience*, 31(21), 7670–7681. <https://doi.org/10.1523/JNEUROSCI.0629-11.2011>
- Zele, A. J., Adhikari, P., Cao, D., & Feigl, B. (2019). Melanopsin driven enhancement of cone-mediated visual processing. *Vision Research*, 160, 72–81. <https://doi.org/10.1016/j.visres.2019.04.009>
- Zhao, X., Stafford, B. K., Godin, A. L., King, W. M., & Wong, K. Y. (2014). Photoresponse diversity among the five types of intrinsically photosensitive retinal ganglion cells. *The Journal of Physiology*, 592(7), 1619–1636. <https://doi.org/10.1113/jphysiol.2013.262782>

## SUPPORTING INFORMATION

Additional supporting information may be found online in the Supporting Information section at the end of this article.

**How to cite this article:** Sonoda T, Okabe Y, Schmidt TM. Overlapping morphological and functional properties between M4 and M5 intrinsically photosensitive retinal ganglion cells. *J Comp Neurol*. 2020;528:1028–1040. <https://doi.org/10.1002/cne.24806>